RSC Advances

PAPER

View Article Online
View Journal | View Issue

Check for updates

Cite this: *RSC Adv.*, 2025, **15**, 31884

AC corona aging behavior and performance comparison of HTV silicone rubber, cycloaliphatic epoxy resin, and glass fiber-reinforced epoxy used in composite insulators

Yuelin Liu, Wendong Li,* Shiyin Zeng, Xinyi Yan, Haoyan Liu, Yuanyang Liu and Guanjun Zhang*

Cycloaliphatic epoxy resin (CEP) is a promising candidate for rigid housings in high-voltage composite insulators due to its superior hardness, water resistance, and interfacial adhesion compared with conventional high-temperature vulcanized silicone rubber (HTV-SR). However, the long-term insulation degradation mechanisms of CEP under corona discharge are still not fully understood. In this study, CEP, HTV-SR, and glass fiber-reinforced epoxy (GFRP) were subjected to AC corona aging using a multi-needle plate electrode. Surface morphology, chemical structure, and electrical properties were comprehensively evaluated. The results show that all three materials experienced progressive surface cracking and increased roughness during aging, leading to notable reductions in hydrophobicity, resistivity, and DC flashover voltage. Surface degradation was found to be more significant than bulk degradation. CEP maintained a denser microstructure containing carbonized residues and inorganic fillers, and exhibited less severe cracking compared with HTV-SR. FTIR and XPS analyses revealed that CEP underwent epoxy ring opening, accumulation of polar groups, and surface carbonization, accompanied by a marked decrease in the C/O ratio and deterioration of dielectric properties. In comparison, HTV-SR developed a protective silica-like layer through oxidative crosslinking, which helped preserve its structural integrity and insulation performance. GFRP suffered the most severe deterioration, including resin erosion and glass fiber exposure. Principal component analysis (PCA) of multiple performance indicators confirmed that CEP demonstrated aging resistance comparable to HTV-SR and superior to GFRP. These findings provide a theoretical foundation for the engineering application of CEP in high-voltage composite insulators.

Received 18th July 2025
Accepted 27th August 2025

DOI: 10.1039/d5ra05182g

rsc.li/rsc-advances

1 Introduction

Composite insulators are widely employed in power systems due to their excellent contamination flashover resistance and light weight.[1,2] Currently, high-temperature vulcanized silicone rubber (HTV-SR) is commonly used for sheds and sheaths, while glass fiber-reinforced epoxy (GFRP) serves as the core rod material.[3] Although traditional composite insulators demonstrate outstanding initial performance upon installation, their long-term reliability is limited by the inherent mechanical properties of silicone rubber and interfacial defects between the core rod and the sheath. These issues frequently result in bird pecking damage,[4] abnormal heating,[5] and decay-like fracture of core rod,[6] posing serious risks to the safe and stable operation of the power grid.

In recent years, cycloaliphatic epoxy resin (CEP) has attracted attention as a promising insulating material. Unlike conventional bisphenol A-based epoxy resins, CEP lacks aromatic rings and offers superior thermal stability, weather resistance, and electrical properties.[7] Hydrophobic CEP materials have been developed by incorporating functional additives,[8] and have been successfully applied as shed and sheath materials in novel rigid composite insulators. Studies have shown that these insulators exhibit excellent hydrophobicity, low water permeability, and favorable mechanical properties in tests such as water diffusion,[9] water ingress,[10,11] UV exposure,[12] and interfacial resistance.[13] These advantages help to mitigate typical failure modes of traditional silicone rubber insulators, including overheating and decay-like aging caused by interfacial degradation. As a result, CEP-based materials show improved adaptability to harsh environments such as high humidity, sandstorms, and bird pecking.

As the outer insulation layer of composite insulators, the weather shed is continuously exposed to atmosphere and

---

State Key Laboratory of Electrical Insulation and Power Equipment, Xi'an Jiaotong University, Xi'an, Shaanxi 710049, China. E-mail: wendongli@xjtu.edu.cn; gjzhang@xjtu.edu.cn

subjected to multiple stress factors such as corona discharge, ultraviolet radiation, and hygrothermal cycling.[14,15] Among these, corona discharge generates high-energy particles and reactive oxidative species, which can break molecular chains and reorganize functional groups, ultimately leading to a reduction in material service life. To date, extensive research has been conducted on the corona aging behavior of HTV-SR. M. Bi *et al.*[16] investigated the corona aging of HTV-SR under varying humid-thermal conditions, revealing that increased humidity and surface contamination promote the formation of polar groups, resulting in rapid hydrophobicity loss and significant deterioration of insulation performance. Y. Zhu *et al.*[17] studied the hydrophobicity loss and recovery process of HTV-SR under contaminated conditions before and after corona aging, highlighting the dynamic evolution of surface polar functionalities. S. Zeng *et al.*[18] further reported that alternating thermal stress facilitates crack formation in HTV-SR, promoting the diffusion of corona byproducts and water molecules into the bulk, thereby accelerating aging. In addition, aluminum hydroxide fillers commonly used in silicone rubber tend to undergo dehydration and migration under high-temperature corona stress, forming powdery surface deposits through chemical reactions, which further impair tracking and erosion resistance.[19]

By contrast, bisphenol A-based epoxy resins are prone to severe degradation under corona discharge. G. Pang *et al.*[20] demonstrated that increasing corona intensity and aging time lead to higher dielectric constant and loss tangent in GFRP core rods, accompanied by main-chain scission of the epoxy matrix, ester hydrolysis, and curing agent failure, ultimately weakening the fiber–resin interfacial bonding. C. Zhang *et al.*[21] conducted systematic investigations on epoxy resin degradation under bipolar square-wave electric fields, including aging morphology, surface charge traps, and service life, and observed that surface microstructural damage and accumulation of polar groups markedly reduce the electrical performance.

Overall, conventional HTV-SR and bisphenol A-based epoxy materials commonly suffer from hydrophobicity loss, surface structural degradation, and deterioration in mechanical and electrical properties under corona discharge. However, the aging mechanisms, structural evolution, and corona resistance of emerging CEP remain insufficiently studied. Moreover, direct comparative analyses with existing HTV-SR and GFRP materials under identical service conditions are still lacking.

In this study, a multi-needle plate electrode was employed to conduct accelerated corona aging tests on HTV-SR, CEP, and GFRP used in composite insulators. The surface morphology, structural characteristics, and electrical property changes of the three materials under different corona durations were systematically analyzed, revealing the degradation mechanism of CEP under corona discharge. In addition, a PCA-based multi-parameter evaluation framework was established, enabling a comparative assessment of the corona aging resistance among the three materials. The findings provide theoretical guidance for the optimized selection of composite insulator materials in power systems.

2 Experimental details

2.1 Sample preparation

The HTV-SR samples used in this study were provided by Xiangyang Guowang Composite Insulators Co., Ltd. As shown in Fig. 1(a), the polymer consists of a polydimethylsiloxane (PDMS) backbone with a small amount of vinyl-functionalized side chains. Inorganic fillers such as carbon black and aluminum hydroxide (ATH) are typically incorporated to enhance tracking resistance and thermal stability. The shed material of the novel rigid composite insulator was supplied by Beijing Core Technology Co., Ltd. and fabricated using the automatic pressure gelating (APG) technique.[22] The matrix of this material is CEP, whose representative molecular structure is illustrated in Fig. 1(b). During curing, CEP crosslinks with an anhydride curing agent to form a dense three-dimensional network. GFRP samples were used as representative core rod materials and were prepared using a bisphenol-A epoxy resin matrix which illustrated in Fig. 1(c).

To ensure consistency across all test conditions, the three types of materials were processed into disc-shaped specimens with a diameter of 100 mm and a thickness of 0.2 mm. Prior to testing, the sample surfaces were cleaned using non-woven fabric soaked in anhydrous ethanol to remove dust and grease. The cleaned samples were then air-dried and sealed in clean, dry containers to minimize the influence of moisture absorption and contamination on subsequent experiments.

2.2 Corona discharge system

The AC corona aging platform used in this study consists of a power-frequency high-voltage source, a constant-temperature and constant-humidity test chamber, a multi-needle-plate electrode system, and a discharge parameter monitoring module. A schematic diagram of the overall setup is shown in Fig. 2(a). The upper electrode of the multi-needle system is fabricated from a 5 mm thick aluminum plate and comprises nine independent discharge units with a center-to-center spacing of 120 mm to avoid mutual coupling interference during discharge. Each unit contains 91 stainless steel needles with a tip radius of curvature of approximately 50 μm. The detailed configuration of the needles is illustrated in Fig. 2(b). This design is an optimized extension of the three-ring needle array recommended by CIGRE D1.14.[23] The hexagonal configuration was adopted to provide more isotropic field coverage and to minimize edge effects compared with square or linear arrangements.

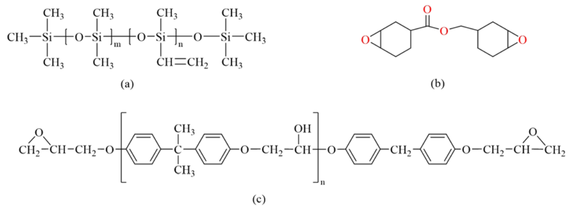

Fig. 1 Chemical structures of the materials. (a) polydimethysiloxane; (b) cycloaliphatic epoxy resin; (c) bisphenol A type epoxy resin.

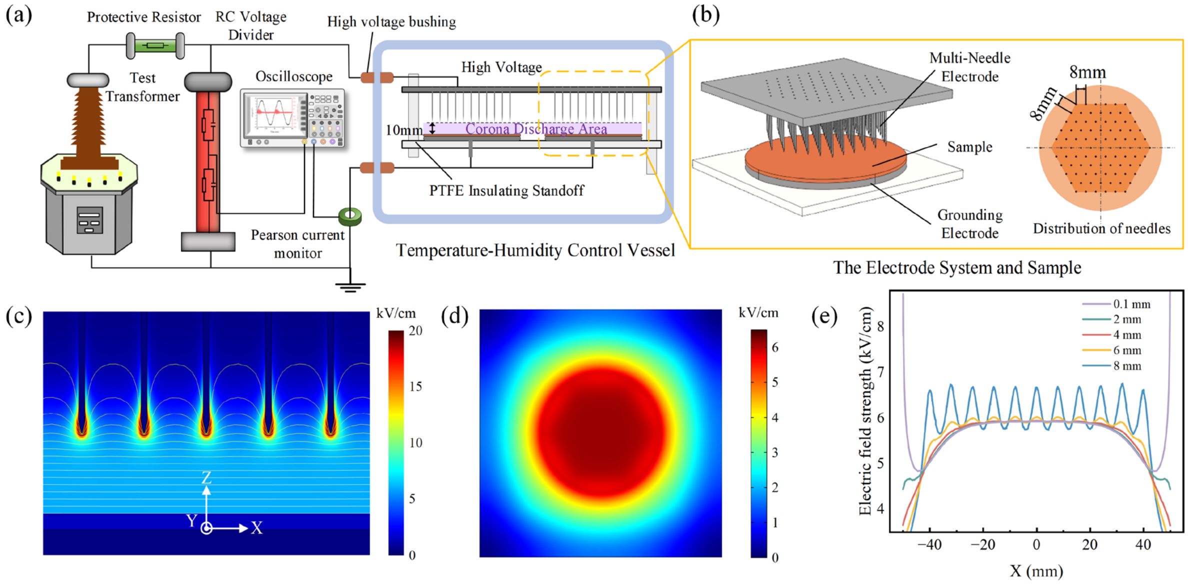

Fig. 2 Accelerated corona aging test platform: (a) schematic diagram; (b) structure of the multi-needle-plate electrode; (c) electric field distribution in the longitudinal section of the needle array; (d) electric field distribution on the sample surface; (e) electric field strength between the needle tips and the sample surface at $y = 0$ mm.

The lower electrode is a 4 mm thick circular aluminum plate and the two electrodes are fixed using polytetrafluoroethylene (PTFE) supports. The needle-plate gap can be continuously adjusted from 2 mm to 40 mm to accommodate test samples of different thicknesses and to study the influence of gap distance on electric field distribution.

To verify the electric field uniformity of the electrode system, a three-dimensional simulation model was established using COMSOL Multiphysics. The boundary conditions were defined as +6 kV RMS applied to the upper electrode and the lower electrode grounded. Fig. 2(c) and (d) show the simulated electric field distribution in the longitudinal section of the needle array and on the sample surface, respectively. The results indicate that within a central region of 30 mm radius, the surface electric field remains stable in a narrow range of 5.9 ± 0.01 kV cm^{-1}. As shown in Fig. 2(e), the field distribution plotted at $y = 0$ mm corresponds to the central region beneath the electrode array, where the overlapping fields from adjacent needles produce a relatively uniform distribution. At positions closer to the electrode edges, the field distribution exhibits greater non-uniformity due to reduced overlap between needles. When the distance between the needle tips and the sample surface is controlled between 8 and 10 mm, the field distribution remains smooth, with a spatial fluctuation gradient less than 3% cm^{-1}.

2.3 Experimental procedure

A voltage regulator was used to control the output of the test transformer at 6 kV RMS, and a multi-needle-plate electrode system was employed to generate a corona discharge environment for accelerated aging of HTV-SR, CEP, and GFRP samples. The temperature inside the test chamber was maintained at 20 °C and 50% relative humidity (RH). Three specimens of each material were placed on the ground electrode in separate compartments, with the vertical distance between the needle tips and the sample surfaces adjusted to 10 mm. The aging durations were set at 0, 100, 200, 300, 400, and 500 hours.

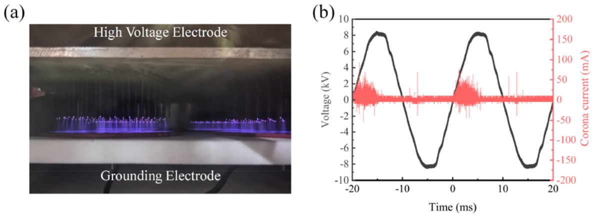

Fig. 3 (a) Corona discharge photograph; (b) voltage–current waveform of corona discharge.

Fig. 3(a) presents a visible-light photograph of the experimental setup. When the ambient light was dim, the corona sheath with a bluish-purple glow was clearly visible around the needle tips. The voltage signal was collected using a 1 : 1000 high-voltage divider, while the current signal was measured by a Pearson current transformer (frequency response range: 0.1 Hz–20 MHz). A typical voltage–current waveform is shown in Fig. 3(b), where the positive half-cycle current peak reaches up to 50 mA, which is clearly higher than that in the negative half-cycle, reflecting the field enhancement effect at the anode needle tips.

2.4 Characterization

2.4.1 Morphological and structural characterization. The surface morphology of the samples was examined using a scanning electron microscope (SEM, ZEISS Sigma 360, Germany). The static water contact angle was measured using an optical contact angle goniometer (KRÜSS DSA100, Germany). Measurements were conducted 10 days after the completion of corona aging. For each sample, five measurements were performed at different surface locations. The chemical bonding structure was analyzed by Fourier transform infrared spectroscopy (FTIR, Thermo Fisher Scientific Nicolet IZ10, USA), with a scanning range from 500 to 4000 cm^{-1} and a resolution of 4 cm^{-1}. X-ray photoelectron spectroscopy (XPS, Thermo Scientific K-ALPHA, USA) was used to qualitatively and quantitatively analyze the surface elemental composition and chemical states. Thermogravimetric analysis (TGA, METTLER TOLEDO TGA/DSC 1, Switzerland) was carried out from room temperature to 800 °C at a heating rate of 10 °C min^{-1} under a nitrogen atmosphere.

2.4.2 Electrical properties. Surface DC flashover voltage was measured using conical electrodes with a diameter of 10 mm and a spacing of 4 mm. The voltage was increased linearly at a constant rate of 1 kV s^{-1} until flashover occurred. Surface resistivity was measured using a high resistance meter (Keithley 6517B, USA) and a three-electrode test fixture (8009). Dielectric spectra were obtained using a broadband dielectric spectrometer (Novocontrol Concept 80, Germany) over a frequency range from 10^{-1} Hz to 10^4 Hz.

3 Results

3.1 Surface morphology and hydrophobicity

Fig. 4 presents the macroscopic surface morphology of the three materials after 500 hours of AC corona aging. Due to the strong electric field concentration at the needle tips, the corona energy was mainly localized in the region directly beneath each tip. As a result, all samples exhibited a circular corona-induced degradation zone on the surface, approximately 4 mm in diameter and centered at the discharge needle. Subsequent characterizations were conducted on the central region of the corona ring.

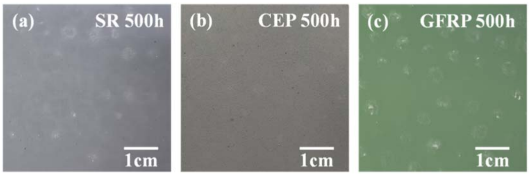

Fig. 4 Photographs of the samples after 500 h of corona aging.

After aging, the surface of the HTV-SR sample was covered with a widespread powdery layer, along with dense mesh-like surface cracks up to several micrometers wide. In contrast, the CEP sample showed much milder surface degradation. Only slight discoloration was observed with increasing aging time, and minor signs of deterioration appeared in localized areas. No extensive cracking or powder formation occurred, and the overall structural integrity was well maintained. The most pronounced changes were observed in the GFRP sample. Its surface gloss diminished, and surface roughness increased. White powdery deposits were also observed, which may be attributed to the degradation of the epoxy matrix, leading to the gradual exposure of embedded glass fibers under prolonged corona discharge.

To further elucidate the evolution of microstructural features during different stages of corona aging, the surface morphologies of samples aged for various durations were examined using SEM, as shown in Fig. 5. The first column displays the unaged surface morphology of each material, while the subsequent columns correspond to aging durations of 100 h, 300 h, and 500 h. All three unaged samples exhibit dense and smooth surfaces without observable microdefects such as cracks, grooves, voids, or particle deposition, indicating that their initial network structures remained intact and can serve as baselines for subsequent degradation analysis.

As corona aging progresses, varying degrees of surface degradation become evident. For HTV-SR, fine cracks begin to appear after 100 h of aging, with widths on the order of several

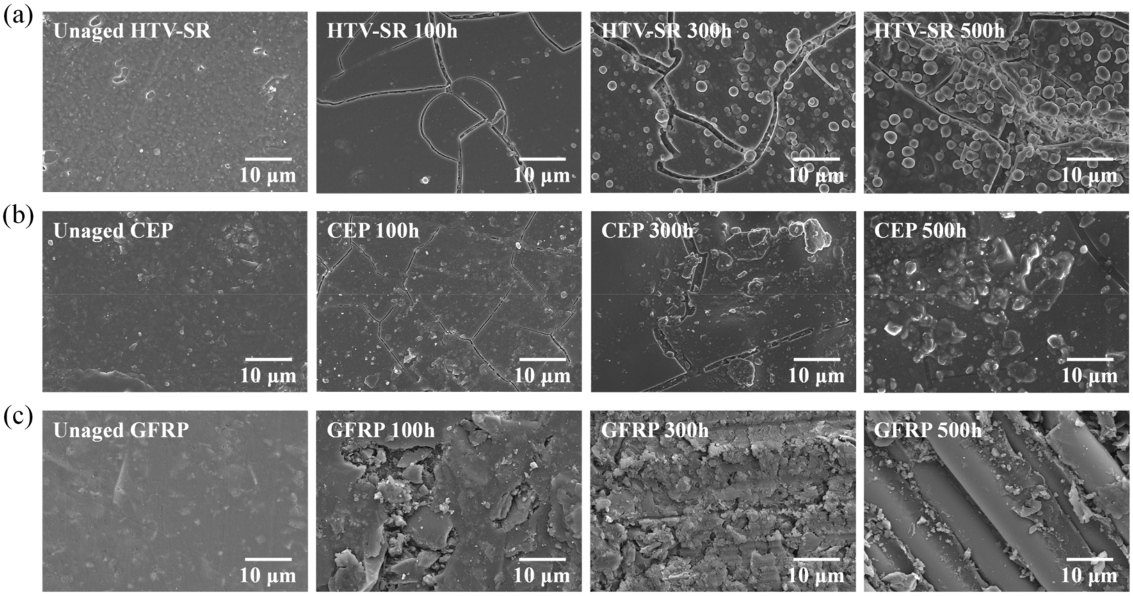

Fig. 5 Microscopic morphology (SEM results) under different corona aging time. (a) HTV-SR; (b) CEP; (c) GFRP.

hundred nanometers. The surface remains relatively flat at this stage. After 300 h, cracks expand notably, reaching widths of 2–3 μm, and groove-like structures form between adjacent cracks. Numerous spherical filler particles, primarily SiO_2, become exposed on the surface, with particle sizes ranging from 100 nm to 1 μm and a few exceeding 1 μm. At 500 h, partial surface delamination occurs, cracks develop into a dense, interlaced network, and surface roughness increases markedly. The fillers are almost entirely exposed and show a more uniform size distribution, with an average diameter of approximately 2–3 μm, indicating the onset of severe degradation.

In contrast, the CEP samples exhibit much higher morphological stability. Throughout the aging process, only isolated microcracks appear on the CEP surface, with smaller widths and depths than those observed in HTV-SR. No continuous grooves, powdering, or large-area peeling are detected. The surface remains largely dense and intact. After 300 h of aging, irregular blocky or angular particle aggregates begin to form on the surface. These are presumed to be re-deposited products of carbonized resin and inorganic fillers caused by high-energy ion bombardment.

For the GFRP samples, the degradation process is notably faster than in the other two materials. After 100 h of aging, partial delamination of the resin layer is observed, although the glass fibers remain covered. By 300 h, the delaminated area expands substantially, and fiber bundles become partially exposed. After 500 h, the epoxy matrix is almost completely degraded, leading to large-scale exposure of the glass fibers and the formation of severe structural defects.

Fig. 6 shows the variation in static water contact angle. Overall, all materials exhibited a decreasing trend in contact angle with prolonged aging, indicating a continuous deterioration of surface hydrophobicity under corona stress. However, the extent of degradation and the ability to recover varied considerably among the materials. In the unaged state, both HTV-SR and CEP exhibited excellent initial hydrophobicity, with contact angles of 120.7° and 116.8°, respectively. After 500 hours of aging, their contact angles decreased to 104.5° and 100.6°, respectively. Although reduced, these values remained relatively high, suggesting that both materials possess a certain degree of hydrophobic recovery capability. The reduction in water contact angle is governed by both the evolution of surface roughness and the transformation of surface chemistry, with chemical modifications considered the dominant factor under corona aging.

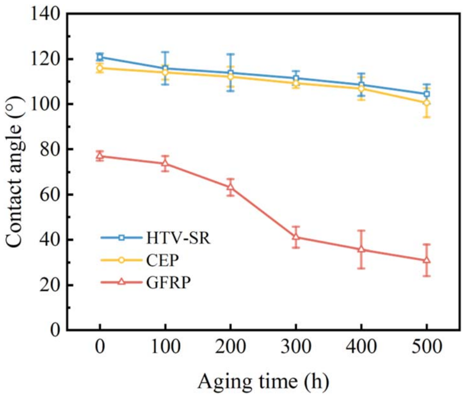

Fig. 6 Static water contact angle as a function of corona aging duration.

HTV-SR contains a high density of highly hydrophobic Si–CH_3 side groups, which impart ultra-low surface energy and result in excellent initial water repellency. Corona discharge breaks Si–CH_3 bonds and oxidizes them into polar groups, causing a rapid decline in contact angle. However, a large amount of low molecular weight (LMW) siloxanes remain in the silicone rubber matrix. These molecules can slowly migrate toward the surface along a concentration gradient after aging, rearranging to form a hydrophobic overlayer, thereby partially restoring the contact angle.

The main chain of cycloaliphatic epoxy resin consists of saturated alicyclic structures with high bond energy, making it more resistant to degradation under high-energy particle bombardment. In the modified CEP used in this study, functional additives with special rheological properties were incorporated. After corona stress is removed, these additives can gradually migrate to the surface and mask the oxidized layer, helping to restore the hydrophobic interface and enabling a silicone-like self-recovery mechanism.

In contrast, the GFRP sample exhibited a significantly lower initial contact angle of 77.3°, primarily due to the high polarity of its bisphenol A-based epoxy matrix. Corona aging caused extensive degradation and exposed the intrinsically hydrophilic glass fibers, which tend to form hydrogen bonds with ambient water molecules. As a result, the contact angle dropped to 27.4° after 500 hours of aging, indicating a sharp loss of hydrophobicity. Moreover, this material lacks hydrophobic side groups and migratable molecules, leading to an irreversible surface aging without self-recovery capability.

3.2 Chemical and thermal characterization

To evaluate the evolution of surface chemical structures, FTIR analysis was performed, and Table 1 summarizes the characteristic absorption peaks corresponding to the main functional groups.

Fig. 7(a) shows the infrared spectra of HTV-SR. With increasing corona exposure time, the characteristic absorption

Table 1 Characteristic absorption bands and corresponding functional groups identified in the FTIR spectra

Wavenumber (cm^{-1})	Absorbance
3700–3200	O–H
2970–2920	C–H in CH_3
1736	C=O in ester
1608, 1508	Aromatic structure
1270–1255	Si–CH_3
1182	C–C in aliphatic
1081	C–O–C in aliphatic
1100–1000	Si–O–Si
840–790	$Si(CH_3)_2$

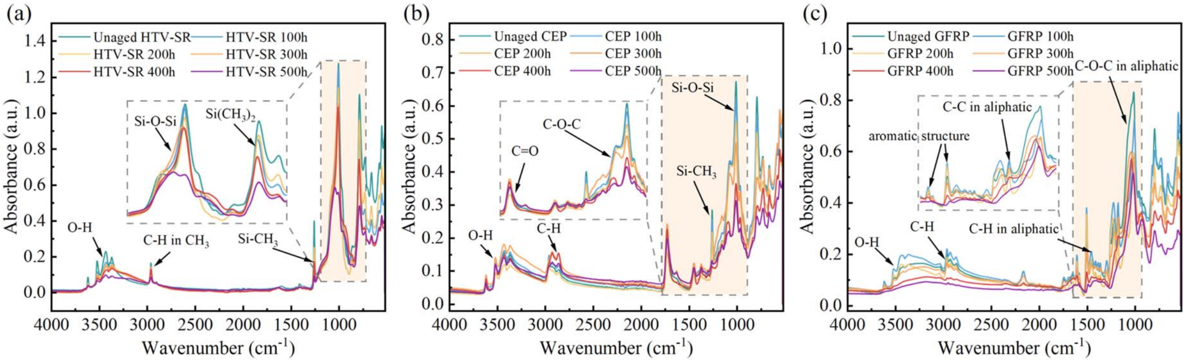

Fig. 7 FTIR spectra of the materials under different aging time. (a) HTV-SR; (b) CEP; (c) GFRP.

peaks of Si–O–Si, Si–CH_3 and $Si(CH_3)_2$ continuously weaken, indicating synergistic degradation involving main chain scission and methyl group oxidation. Notably, after 500 h of aging, the peak area of Si–CH_3 decreases by approximately 60% compared to the unaged state, reflecting severe oxidation and transformation of methyl groups into polar species such as Si–OH. This oxidation pathway is further supported by the broadening of the –OH absorption band, suggesting gradual hydroxyl enrichment on the surface. However, the intensity of the –OH peak does not monotonically increase; instead, it exhibits nonlinear fluctuations throughout the aging process. This phenomenon may result from the dehydration of ATH fillers under high-energy plasma and localized heating, consuming hydroxyl groups and competing with the oxidation-induced formation of Si–OH, thus leading to complex OH band behavior.

Fig. 7(b) displays the FTIR spectra of CEP samples. The characteristic peaks of C–H and C–O–C exhibit varying degrees of attenuation, indicating epoxy ring opening and ether bond breakage. The C═O absorption peak initially increases and then decreases, with a new shoulder appearing at a lower wavenumber, likely due to the formation of unsaturated carbonyl products. The C–H absorption peak in CEP is broader and occurs at a lower wavenumber than in HTV-SR, corresponding to the cycloaliphatic structure and methylene C–H stretching. Similar to HTV-SR, the peaks of Si–O–Si and Si–CH_3 groups in CEP also decrease, with an even greater reduction. This is mainly because these groups in CEP originate from silicone prepolymer grafted onto the epoxy backbone, which has lower bond energy and is more susceptible to breakage under corona stress. Notably, after 500 hours of aging, the main C–O–C peak still retains about 70% of its initial intensity, indicating that while oxidation occurs at the surface of CEP, the internal main chain structure largely remains intact. The emergence of new carbonyl shoulders suggests secondary oxidation of hydroxyl groups into carboxylic acids and aldehydes, accompanied by partial esterification or crosslinking. These chemical transformations accelerate surface carbonization but preserve the bulk integrity of the cycloaliphatic backbone.

Fig. 7(c) illustrates the results of GFRP samples. In contrast to CEP, GFRP contains aromatic structures. During corona aging, peaks corresponding to methyl, aliphatic, and aromatic groups exhibit an overall decline. In particular, the intensity of the C–O–C skeletal vibration decreases by more than 40% after 500 h, reflecting extensive hydrolysis and degradation of the resin matrix, leading to severe molecular chain scission. The O–H absorption initially increases within the first 200 h due to matrix hydrolysis and hydroxyl formation but subsequently decreases between 300 and 500 h as matrix disintegration reduces the interfacial amorphous phase. This irreversible molecular degradation process aligns well with the sharp decline in hydrophobicity observed in the contact angle measurements, further confirming the deep chain scission and interfacial destabilization mechanisms induced by corona discharge. Moreover, the breakdown of aromatic rings under

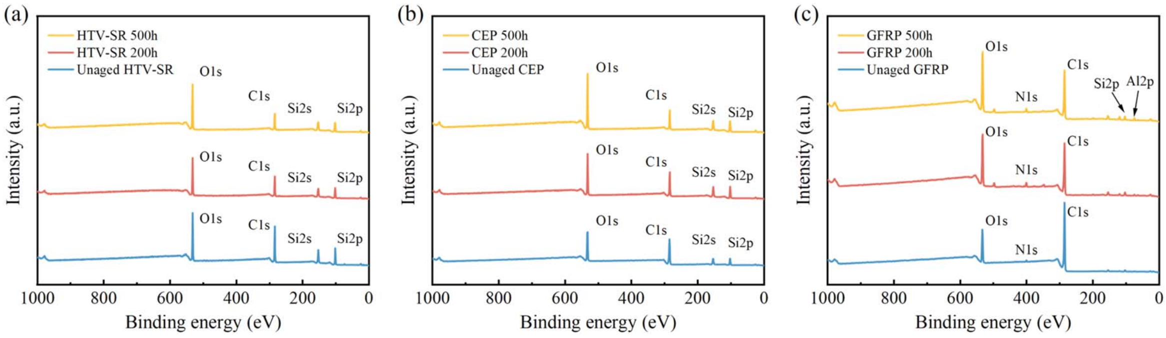

Fig. 8 XPS survey spectra of the three materials after corona aging for 0 h, 200 h, and 500 h. (a) HTV-SR; (b) CEP; (c) GFRP.

oxidative attack generates phenolic and quinone-type intermediates, which destabilize the crosslinked epoxy network.

Fig. 8 presents the XPS survey spectra of the three materials aged for 0 h, 200 h, and 500 h. All spectra were calibrated using the C 1s binding energy at 284.8 eV. For HTV-SR and CEP, dominant peaks corresponding to O 1s, C 1s, Si 2s, and Si 2p were observed. In GFRP, in addition to prominent C 1s and O 1s signals, minor peaks of Si 2p, N 1s, and Al 2p were detected, attributed to the glass fiber reinforcement and residual fillers.

Table 2 summarizes the atomic percentages of major elements and the variation of the C/O atomic ratio for each material. The decrease in C/O ratio after corona aging is primarily due to surface oxidation initiated by reactive oxygen species (ROS) generated in atmospheric plasma, including atomic oxygen, ozone, and hydroxyl radicals. These species readily attack the polymer chains, leading to bond scission and the evolution of carbon-oxygen structurals. Specifically, for HTV-SR, the C/O ratio decreased from 0.64 to 0.32 after 500 h, with a 13% reduction in carbon content, while the Si content remained relatively stable at around 14%, suggesting extensive oxidation of methyl groups to silanol or silicon oxides. For CEP, a similar trend was observed, with the C/O ratio decreasing from 0.78 to 0.32, indicating notable carbon backbone degradation and oxidation. Meanwhile, the surface Si content increased from 8.63% to 13.22%, implying that filler particles became exposed and involved in subsequent oxidation as the matrix degraded. In contrast, GFRP exhibited the most pronounced decrease in C/O ratio, from 1.57 to 0.64, along with the greatest carbon loss.

Table 2 Atomic percentages of major elements and corresponding C/O ratios in the three materials at different stages of corona aging

Sample	Aging time	C	O	Si	C/O
HTV-SR	0 h	33.33%	52.32%	14.35%	0.64
	200 h	27.76%	57.47%	14.77%	0.48
	500 h	20.93%	65.49%	13.58%	0.32
CEP	0 h	40.05%	51.03%	8.93%	0.78
	200 h	32.53%	54.55%	12.92%	0.60
	500 h	20.82%	65.96%	13.22%	0.32
GFRP	0 h	60.45%	38.39%	1.16%	1.57
	200 h	43.97%	53.56%	2.48%	0.82
	500 h	38.03%	59.35%	2.62%	0.64

Fig. 9 presents the peak fitting results of Si 2p for HTV-SR, and C 1s for both CEP and GFRP samples. The relative atomic concentrations of the fitted chemical structures are summarized in Tables 3–5.

For HTV-SR, the Si 2p spectrum reveals three typical silicon oxidation states: Si(–O)$_2$, Si(–O)$_3$, and Si(–O)$_4$, with binding energies of approximately 102.1 eV, 102.8 eV, and 103.4 eV,[24] respectively. Si(–O)$_2$ corresponds to partially oxidized siloxane backbone structures, while Si(–O)$_4$ indicates the formation of SiO$_2$ due to extensive oxidation or filler migration.[25] With

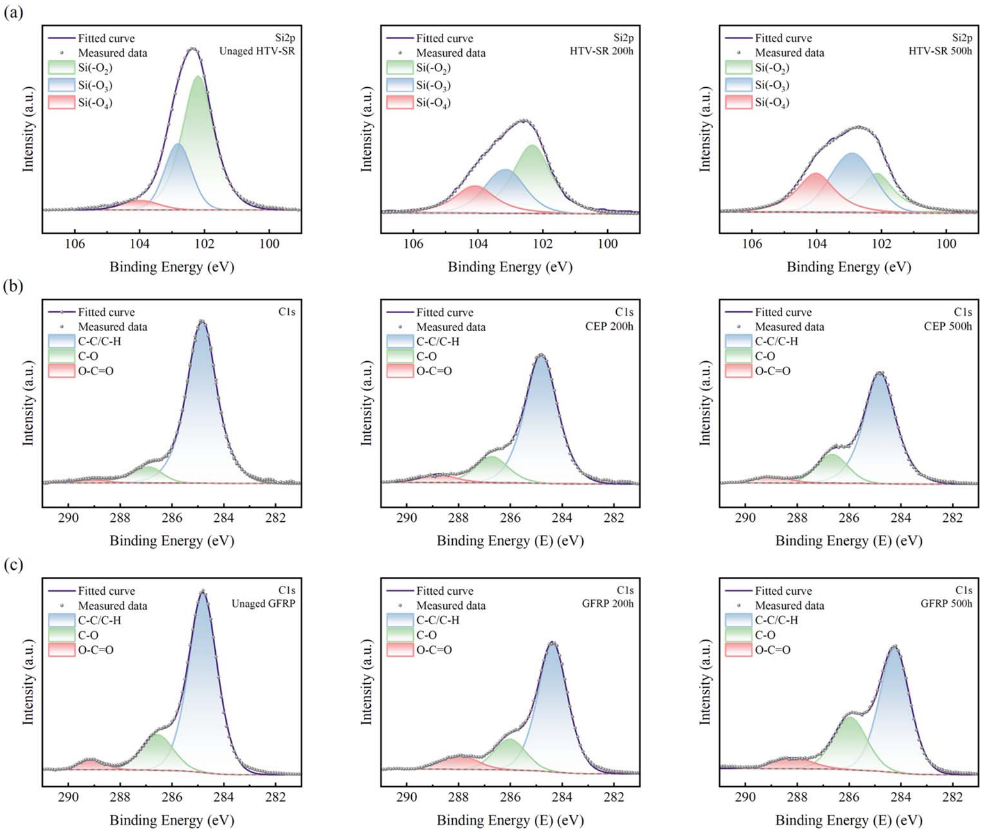

Fig. 9 High-resolution XPS spectra and peak fitting results of corona-aged samples: (a) Si 2p spectrum of HTV-SR; (b) C 1s spectrum of CEP; (c) C 1s spectrum of GFRP.

Table 3 Relative contents of different silicon oxidation states in HTV-SR based on Si 2p peak fitting

Aging time	Si(–O)$_2$	Si(–O)$_3$	Si(–O)$_4$	SiO$_x$
0 h	67.62%	28.29%	4.09%	32.38%
200 h	47.52%	36.29%	16.19%	52.48%
500 h	28.36%	38.73%	32.91%	71.64%

Table 4 Relative atomic concentrations of carbon functional groups in CEP obtained from C 1s peak fitting

Aging time	C–C/C–H	C–O	O–C=O
0 h	87.4%	9.31%	3.29%
200 h	79.72%	16.08%	4.2%
500 h	76.11%	19.17%	4.72%

Table 5 Relative atomic concentrations of carbon functional groups in GFRP obtained from C 1s peak fitting

Aging time	C–C/C–H	C–O	O–C=O
0 h	79.11%	17.04%	3.85%
200 h	73.02%	17.81%	9.17%
500 h	63.98%	28.94%	7.07%

increasing corona aging time from 0 to 500 h, the proportion of Si(–O)$_2$ continuously decreases by 40%, while that of Si(–O)$_4$ significantly increases to over 32%. This trend suggests that under the combined effects of corona discharge and oxidative stress, methyl side groups in PDMS are gradually oxidized into Si–OH, which subsequently transform into condensed Si–O–Si structures under localized heating, explaining the simultaneous presence of oxidation and re-crosslinking. The interplay of these two processes progressively builds a silica-like protective layer, consistent with the white powder deposits observed macroscopically.

For CEP, the C 1s spectra can be deconvoluted into three carbon-based chemical states at different binding energies.[26] C–H and C–C bonds are represented by the sub-peak at 284.8 eV, corresponding to nonpolar carbon chains or cycloaliphatic backbones. C–O bonds at 286.7 eV are mainly attributed to epoxy and ether linkages. O–C=O bonds at 289 eV are associated with oxidation products such as carboxylic acids and esters. As the aging duration increased from 0 to 200 h, the peak area of C–C/C–H decreased by approximately 8%, indicating the cleavage of nonpolar segments in the main chain.[27] Concurrently, the intensities of the C–O and O–C=O peaks increased markedly, reflecting the progression of oxidation reactions. After further aging to 500 h, the C–O peak growth tended to plateau, and the O–C=O component showed no significant increase, suggesting that the degree of oxidation had reached saturation and no deep carboxylation degradation occurred.

For GFRP samples, the C 1s spectra resemble those of CEP but exhibit more pronounced changes. In the unaged state, the C–C/C–H peak dominates, indicating high contents of aromatic and aliphatic carbon chains in the epoxy matrix. After 200 h of aging, this peak rapidly decreases, while C–O and O–C=O components increase concurrently, signifying severe chain scission and accumulation of polar functional groups induced by corona discharge. At 500 h, the combined share of C–O and O–C=O exceeds 35%, noticeably higher than that of CEP under the same conditions. This indicates that the bisphenol-A aromatic epoxy resin used in GFRP is more susceptible to breakage and oxidation under strong electric fields. Furthermore, the exposure of the glass fiber interface aggravates surface polarization and oxidation reactions, leading to poorer structural stability.

Fig. 10 shows the TGA results of the three materials. In the unaged state, HTV-SR exhibits a two-stage thermal decomposition behavior. The first stage occurs between 200 and 350 °C corresponding to the breakdown of Si–CH$_3$ groups and the volatilization of cyclic siloxanes. The second stage, from 350–550 °C, is primarily attributed to the decomposition of the Si–O–Si backbone, with a maximum derivative thermogravimetric (DTG) peak near 460 °C. At 800 °C, the residual mass is approximately 50%, mainly due to inorganic fillers. After 500 h of corona aging, the initial decomposition temperature decreases from 286 °C to 274 °C, while the residual mass increases to 54%. This shift indicates that the oxidized surface layer introduced by corona discharge creates volatile defects at lower temperatures but forms a dense network structure at higher temperatures, effectively suppressing deep decomposition and volatilization. This interpretation is consistent with the increased Si(–O)$_4$ content observed in the XPS spectra and the reduced Si–CH$_3$ peaks in FTIR.

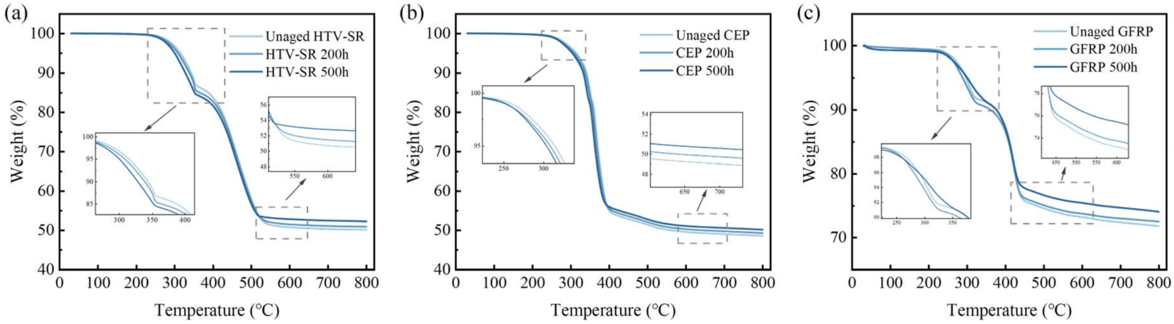

Fig. 10 TGA curves of three samples before and after corona aging. (a) HTV-SR; (b) CEP; (c) GFRP.

CEP demonstrates a single-step thermal degradation process, with major weight loss occurring between 300 and 500 °C. The DTG peak around 362 °C corresponds to the thermal decomposition of epoxy groups, ester bonds, and aliphatic side chains. Less than 5% of weight loss occurs below 300 °C, primarily due to the release of adsorbed moisture and residual LMW oligomers. Above 500 °C, the mass remains nearly stable, with a final residue of about 45%. After corona aging, the initial decomposition temperature decreases from 312 °C to 304 °C, indicating that ring-opening and carbonyl formation caused by mild oxidation enhance volatilization at lower temperatures, thus reducing thermal stability. The overall resin mass fraction also declines from 48.7% to 46.5%, reflecting gradual matrix degradation.

The GFRP samples also exhibit a dual-peak thermal decomposition profile. The first stage (250–350 °C) is mainly due to the initial decomposition of the epoxy matrix, while the second stage (350–550 °C) corresponds to further degradation of the network structure and the rupture of interfacial bonds between the resin and glass fibers.[28] In the unaged state, two DTG peaks are observed at approximately 311 °C and 420 °C, representing matrix decomposition and interfacial debonding, respectively. After 500 h of aging, the residual mass increases from 73% to 76%, likely due to interfacial carbonization. Meanwhile, the downward shift in decomposition temperatures indicates that the matrix structure has undergone significant degradation.

3.3 Electrical properties

To evaluate the impact of corona aging on insulation performance, DC flashover voltage tests were conducted on the three materials. The results were fitted using the Weibull distribution function,[29,30] as expressed in eqn (1). The fitting curves are presented in Fig. 11:

$$P(V_s) = 1 - \exp\left[-\left(\frac{V_s}{\alpha}\right)^{\beta}\right] \tag{1}$$

where α is the scale parameter, representing the characteristic flashover voltage at a cumulative probability of 63.2%, which reflects the typical withstand capability under the given condition. β is the shape parameter, indicating the dispersion of failure data.

The results show that in the unaged state, the characteristic flashover voltages of all three materials are approximately 9 kV, with minimal differences. As the aging time increases, the flashover voltages of all samples exhibit a decreasing trend, though the rate and mechanisms of degradation vary considerably. After 500 h of corona aging, the $V_{63.2\%}$ of HTV silicone rubber decreases by approximately 31%. This is mainly attributed to the development of surface microcracks and the exposure of filler particles, which markedly enhance electric field distortion. The crack tips and filler interfaces become prone to triggering local discharges. In addition, oxidation of side chains and the migration loss of LMW PDMS reduce shallow trap density, increasing the risk of local charge accumulation and further weakening the material's flashover resistance.

For CEP, the decrease is slightly larger, at around 34%. Although CEP possesses greater initial structural stability, corona-induced ring-opening of epoxy groups and the formation of carbonyls increase the density of surface polar groups. Simultaneously, the surface roughness rises, leading to a more uneven electric field distribution. Oxidation products such as carboxylic acids and esters, which have relatively higher conductivity, may form microchannels in high-field regions and induce premature flashover.

GFRP exhibits the most severe performance degradation, with $V_{63.2\%}$ dropping by up to 41% after 500 h of aging. This is attributed to the extensive hydrolysis and decomposition of the

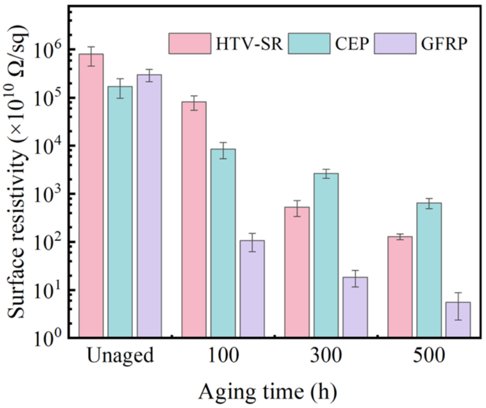

Fig. 12 Surface resistivity of the three samples under different aging time.

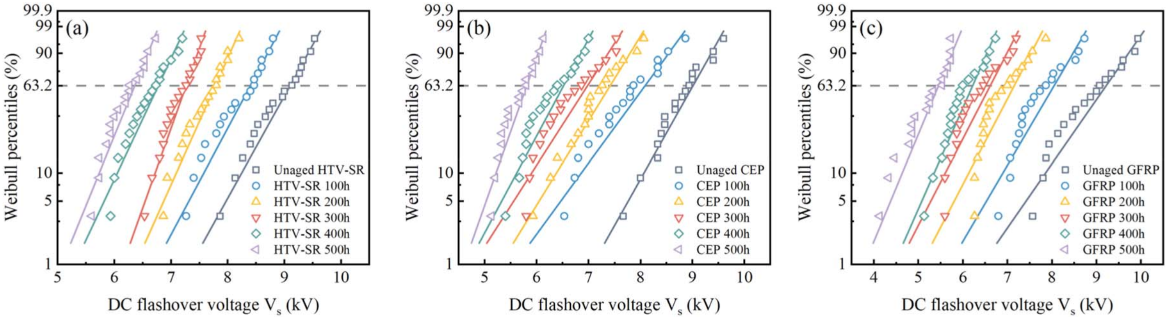

Fig. 11 Weibull distribution curves of DC flashover voltage under different aging time. (a) HTV-SR; (b) CEP; (c) GFRP.

bisphenol-A epoxy matrix under corona exposure, which leads to interfacial failure between the glass fibers and the resin matrix, forming numerous void defects. Additionally, the exposed glass fibers and localized carbonized products create tip effects that intensify local electric field concentrations, greatly increasing the likelihood of surface discharge pathways and severely compromising the overall insulation performance.

To further assess the surface defect evolution and backbone stability of the materials, both surface and volume resistivities were measured. Fig. 12 presents the surface resistivity results. After 500 h of corona aging, the surface resistivity of HTV-SR decreased from 10^5 Ω sq^{-1} to 10^2 Ω sq^{-1}, spanning three orders of magnitude. Combined with the XPS findings, the corona induced scission and oxidation of surface methyl groups led to the formation of a dense oxidized layer, which exhibited enhanced ionic conductivity under high humidity and energetic particle bombardment. Additionally, the formation of micro-crack networks and exposure of fillers intensified local electric field concentration, accelerating the development of conductive paths along the surface.

For the CEP material, the surface resistivity decreased by approximately two orders of magnitude. This degradation is attributed to the increased density of surface conduction channels resulting from the generation of carbonyl and carboxyl groups, as well as surface roughening, which raises local current density. GFRP exhibited the greatest decline in surface resistivity, with values after aging even lower than those of HTV-SR and CEP. The carbonization and peeling of the epoxy matrix caused by corona discharge, combined with interface degradation, promoted the formation of continuous conductive paths between glass fibers. This was the main reason for the reduction in surface insulation performance.

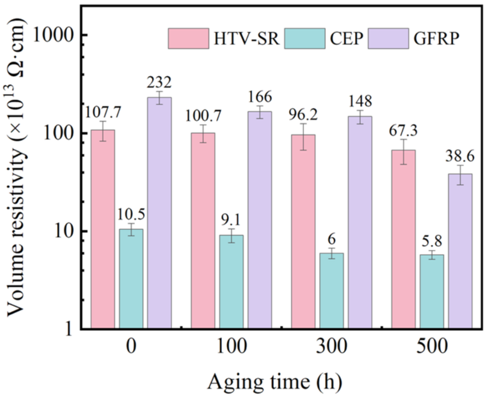

Fig. 13 Volume resistivity of the three samples under different aging time.

The volume resistivity results are shown in Fig. 13. Throughout the aging process, HTV-SR maintained a volume resistivity on the order of 10^{15} Ω cm, indicating that the Si–O–Si backbone and inorganic filler distribution remained stable. The degradation was confined to the top few microns, with negligible impact on the bulk structure. The unaged CEP exhibited an initial volume resistivity of 10^{14} Ω cm, which is one order of magnitude lower than HTV-SR. After 500 h of aging, it decreased to 5.8×10^{13} Ω cm, representing a 40% reduction. FTIR and XPS analyses confirmed that the material underwent ring opening and oxidation during corona discharge. These reactions reduced the crosslinking density and allowed polar groups to migrate into the interior of the material, which in turn weakened its insulation capability. GFRP also showed a pronounced drop in volume resistivity due to resin degradation and filler loss, which created conductive pathways across the thickness direction and facilitated charge transport within the bulk.

Fig. 14 shows the variation trends of the real part of the dielectric constant (ε') and the dielectric loss tangent ($\tan\delta$) for the three materials over the frequency range from 0.1 to 10^4 Hz. For HTV-SR, the ε' of the unaged sample slightly decreases with increasing frequency. This trend is mainly attributed to orientation polarization from the PDMS backbone and limited contributions from interfacial polarization. As aging time increases, ε' at frequencies above 10 kHz remains relatively stable at approximately 4.1, indicating that molecular motion at high frequencies is still constrained by the material's rigidity. In contrast, at 0.1 Hz, ε' rises from 5.07 to 8.94, suggesting that the formation of polar groups enhances low-frequency orientation polarization and reduces the energy barrier for dipole rotation. The $\tan\delta$ initially decreases and then increases, reflecting the combined influence of interfacial polarization and segmental relaxation. After corona aging, $\tan\delta$ increases across all frequencies. For instance, at 0.1 Hz it rises from 0.020 to 0.050, while above 10 kHz the increase remains below 10%, indicating that aging primarily affects surface defects rather than deep structural features.

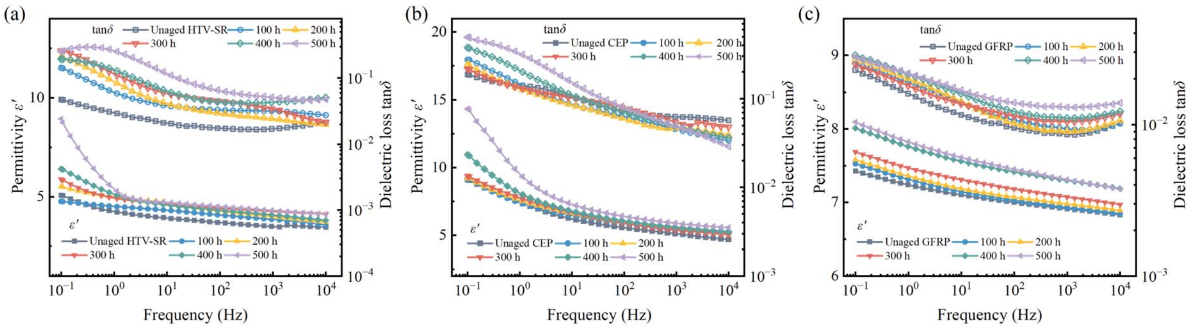

Fig. 14 Dielectric spectra the three materials under different aging time. (a) HTV-SR; (b) CEP; (c) GFRP.

CEP demonstrates a stronger polarization response. The frequency dependence of ε' is similar to that of HTV-SR, but the degree of change is greater. At 0.1 Hz, ε' increases from 9.2 to 14.3 after 500 hours of aging, while changes above 10 Hz are less than 1 unit. This indicates that corona aging significantly enhances low-frequency interfacial polarization and ionic conduction. The $\tan\delta$ continues to rise in the low-frequency region, reflecting accumulated dipole and migration losses. However, at frequencies above 1 MHz, $\tan\delta$ shows a declining trend with prolonged aging, which may be due to reduced contributions from electronic and atomic polarization caused by chain scission and decreased crosslinking density.[31]

GFRP displays a relatively uniform upward shift in ε' across all frequencies. At 0.1 Hz, it increases from 7.4 to 8.1, and at 10 kHz, from 6.8 to 7.2. The overall increase remains within 10%, suggesting that the polarization mechanism is largely unchanged. Nonetheless, enhanced interfacial polarization, charge accumulation, and fiber exposure slightly elevate the overall permittivity. The $\tan\delta$ curve exhibits a characteristic dip at 1 kHz, with a minimum value of 0.0086. After aging, $\tan\delta$ slightly increases across the full spectrum, rising from 0.023 to 0.029 at 0.1 Hz and from 0.010 to 0.014 at 100 kHz. These results indicate that corona aging primarily intensifies dipole rotation and interfacial polarization in the mid-frequency range, with the most noticeable dielectric loss observed near the kilohertz level.

4 Discussions

4.1 Theoretical analysis

The aging of insulating materials under corona discharge is driven by the synergistic erosion of high-energy discharges, ultraviolet radiation, and reactive oxygen species, which leads to distinct degradation pathways in different materials.

Under corona discharge, HTV-SR primarily undergoes two types of structural transformations: main-chain scission and oxidative crosslinking. The high energy impact of plasma particles breaks the Si–O and Si–C bonds in the PDMS backbone, triggering chain depolymerization and reducing the molecular weight. Meanwhile, strong oxidants generated during corona discharge, such as ozone (O_3) and hydroxyl radicals ($^{\bullet}OH$), further initiate oxidative reactions. These reactions gradually convert the originally hydrophobic $Si–CH_3$ side groups into polar Si–OH structures, transforming the surface into a more polar configuration. During this process, volatile by-products such as LMW silanols and formaldehyde fragments may be released, further evidencing chain scission reactions. In addition, the oxidation of $Si–CH_3$ groups disrupts the hydrophobic methyl shielding on the polymer backbone, thereby accelerating the exposure of polar siloxane structures. Some of the generated Si–OH groups undergo condensation or recombination under localized heating, forming new Si–O–Si linkages and establishing a three-dimensional siloxane network.

This molecular transformation is reflected in the FTIR spectra as a progressive decrease in the absorption peaks corresponding to $Si–CH_3$, $Si(CH_3)_2$, and Si–O–Si groups. With increasing oxidation, the surface converts further into silica-like layer, which appears as a white powdery deposit. The increase in O content and the decrease in C content in the XPS spectra confirm this transformation, indicating the concurrent oxidation and loss of organic components and the accumulation of inorganic SiO_2. This dense layer effectively inhibits the ingress of oxygen, moisture, ions, and radicals, thereby slowing down the degradation of deeper layers and helping to preserve the integrity of the polymer backbone.

For CEP, corona aging involves a multi-stage degradation process that includes epoxy ring opening, radical oxidation, and surface carbonization. Initially, the three-membered epoxy rings open under high-energy particle bombardment, generating $–CH_2–OH$ and –OH polar groups. These groups are further oxidized through radical pathways, producing –COOH or –CHO groups. –OOH may also form as intermediates, accelerating side-chain cleavage and the transformation of functional groups. In FTIR spectra, this is evidenced by enhanced C═O peaks and diminished C–O–C and C–H signals. Meanwhile, cleavage of ether linkages and ester bonds occurs under localized discharge and heating, generating LMW acids and aldehydes.

Continued exposure to discharge and localized heating leads to ester bond cleavage, producing low-molecular-weight acids or aldehydes. Some carboxyl and hydroxyl groups undergo condensation reactions, forming unsaturated carbon frameworks that result in carbonaceous residues or highly crosslinked structures. These appear as surface carbon deposits and the formation of conductive pathways, degrading the surface insulation. Simultaneously, the erosion of the organic matrix reveals residual fillers. In XPS spectra, this is indicated by a decrease in C content and an increase in Si and O. The surface gradually transforms into a complex mixture of inorganic residues and carbonized products. SEM images show irregular particulate deposits.

In contrast, GFRP undergoes not only oxidation and degradation of the epoxy matrix but also significant interfacial deterioration and localized discharge-assisted failure. The matrix primarily consists of bisphenol-A type aromatic epoxy, which contains ether linkages, methylene bridges, and aromatic rings. Although the aromatic structure imparts good thermal and mechanical stability, it is susceptible to attack by strong electric fields, ozone, and hydroxyl radicals during corona discharge. This results in chain scission, carbon backbone degradation, and surface carbonization. FTIR and XPS analyses show a decline in methyl, aliphatic, and aromatic features, accompanied by an accumulation of polar functional groups such as hydroxyl and carboxyl, revealing progressive chain breakdown and defect generation. Moreover, the cleavage of ether linkages and methylene bridges promotes the formation of free radicals, which undergo subsequent peroxidation reactions and accelerate the oxidative breakdown of the epoxy network. In addition, the oxidation of aromatic rings produces phenolic and quinone-type intermediates, further weakening the backbone stability and facilitating carbonization.

As matrix erosion intensifies, the interfacial adhesion between resin and glass fibers weakens. Moisture and acidic oxidation products penetrate the interface, leading to silane hydrolysis and interfacial bond rupture. TGA results show a continuous reduction in the organic fraction, indicating persistent matrix decomposition and weight loss. SEM images clearly show exposed glass fibers and interfacial voids. The exposed fibers act as field distortion tips under high electric fields, easily triggering surface discharges and internal electrical tracking. Compared to CEP, GFRP exhibits more irreversible and structurally penetrative degradation during corona aging.

4.2 Comparative analysis of corona aging behavior

To quantitatively evaluate the insulation degradation behavior of the three materials under corona aging, a mathematical model was developed based on experimentally obtained key characterization data to describe the evolution of multiple performance indicators over time. Nine representative parameters were selected as aging degradation indicators, including static contact angle, surface resistivity, volume resistivity, real part of dielectric constant at 50 Hz, dielectric loss tangent, DC flashover voltage, C/O atomic ratio, FTIR absorption peak intensity, and relative content of silicone/epoxy components. These indicators comprehensively reflect surface hydrophobicity, electrical performance, discharge suppression ability, and chemical structure stability.

To avoid the influence of magnitude differences, the surface resistivity was converted to its logarithmic form. Since both the dielectric constant and loss tangent increase with aging, their reciprocals ($1/\varepsilon'$ and $1/\tan\delta$) were used to ensure a consistent interpretation of performance degradation across all parameters. Considering the high sensitivity of PCA to the scale of variables with different dimensions, all raw data were standardized according to eqn (2) prior to analysis.

$$X_{ij} = \frac{x_{ij} - \overline{x_j}}{S_j} \tag{2}$$

in the equation, x_{ij} represents the input variable, $\overline{x_j}$ is the mean, and S_j denotes the standard deviation. After normalization, the covariance matrix of the variables was calculated to evaluate the correlation among indicators. Each element of the matrix was computed using eqn (3).

$$r_{ij} = \frac{1}{n-1}\sum_{k=1}^{n}\left(X_{ki} - \overline{X_i}\right)\left(X_{kj} - \overline{X_j}\right) \tag{3}$$

The contribution rates of each principal component were obtained by calculating the eigenvalues and eigenvectors of the covariance matrix. The eigenvalue indicates the amount of variance captured by a given principal component. A larger eigenvalue reflects a stronger ability of that component to explain the overall variability in the dataset. The corresponding eigenvector determines the direction of the principal component and the contribution coefficients of the original variables.

In this study, the number of principal components was determined using the cumulative variance contribution method. The components were ranked in descending order of contribution, and the top five were selected, as shown in Fig. 15. PC1 and PC2 account for 50.9 percent and 34.6 percent of the total variance, respectively, with a cumulative contribution of 85.6 percent.

In addition, the principal components obtained through PCA were used to project the original high-dimensional data onto a new coordinate system, enabling the construction of a PCA score plot, as shown in Fig. 16. This plot maps the distribution of samples with different aging durations and materials into a low-dimensional principal component space.

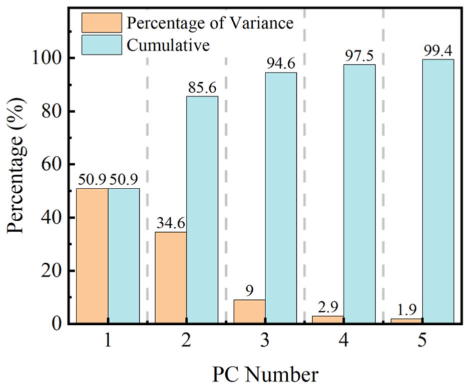

Fig. 15 Variance contribution rates of the top five principal components derived from PCA.

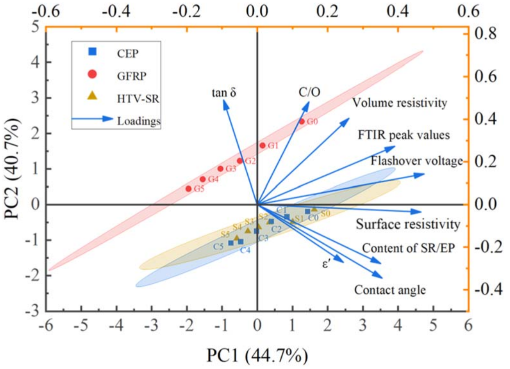

Fig. 16 PCA score and loading plot.

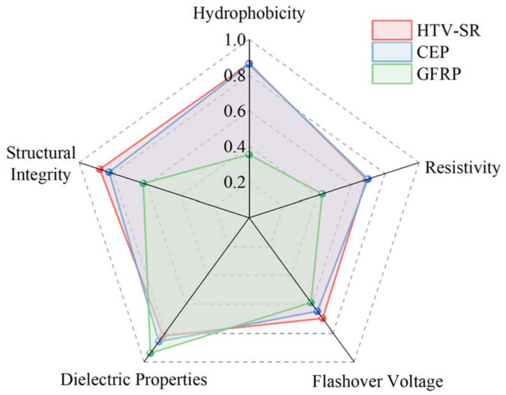

Fig. 17 Radar chart of corona aging resistance.

Table 6 Comparative summary of corona aging studies on polymeric insulating materials

Material	Test conditions	Characteristics	Reference
HTV-SR	AC corona, 8.44 kV, different temperature cycling, 50% RH, 240 h	Chalking, surface defects, oxidation of Si–CH_3 to Si–OH/Si–O–Si, enhanced crosslinking and shallow traps, loss of hydrophobicity	18
Bisphenol A epoxy resin	AC corona, 10 kV, hygrothermal (40–80 °C, 55–95% RH), 100 h	Aromatic degradation, chain scission, severe oxidation, carbonyl/carboxyl formation, resistivity decrease	32
GFRP	AC corona, 20 kV, 25 °C, 80% RH, 480 h	ε' and $\tan\delta$ increased, surface roughening/ablation, epoxy degraded first (C–C, C–H scission, ester hydrolysis), fibers failed later	20
CEP	DC corona, 10 kV, 25 °C, 40% RH, 200 h	Poor hydrophobic recovery, decrease of Si–CH_3/Si–O–Si peaks, surface O/Si increase, C/Al decrease, slight roughening/discoloration	33

The length and direction of each vector indicate the relative weight and influence of the corresponding property on the comprehensive evaluation. The results indicate that unaged samples are generally located in regions with higher PCA scores. As aging time increases, sample points progressively shift toward lower-score regions, reflecting the gradual deterioration of overall material performance.

Comparing the three materials, HTV-SR and CEP exhibit substantial overlap in their PCA score ranges, and their trajectories show only moderate shifts with aging. In contrast, GFRP samples are clearly separated from the other two in score space and show the largest decline in PCA scores over time, indicating a more pronounced degradation in their comprehensive properties under corona aging.

To further visualize the variations in key performance indicators before and after corona aging, a radar chart illustrating the corona aging resistance capabilities of the three materials is presented in Fig. 17. The chart incorporates five representative indicators: hydrophobicity, resistivity, flashover voltage, dielectric properties, and structural integrity. Each parameter is expressed as the characteristic change rate of the 500 h aged sample relative to the unaged one. For the resistivity index, the average change rate of volume and surface resistivity was used. The dielectric index was derived from the average change rates of the real part of the dielectric constant and the dielectric loss tangent. Structural integrity was quantified based on normalized data from SEM, XPS, and TGA analyses.

As shown, both HTV-SR and CEP maintain high performance levels across all five indicators, with CEP exhibiting superior dielectric behavior, while HTV-SR performs slightly better in structural integrity and flashover resistance. In contrast, GFRP shows much weaker performance in all aspects except dielectric properties. Overall, HTV-SR and CEP demonstrate relatively strong aging resistance across multiple dimensions, whereas GFRP undergoes the most severe performance degradation under corona aging.

To provide clearer context, a comparative summary of representative corona-aging studies on polymeric insulating materials is given in Table 6.[18,20,32,33] As seen in the table, most previous works focused on individual degradation parameters, whereas the present study integrates multiple indicators into a PCA-based framework, enabling a quantitative multi-parameter comparison. This highlights the relatively robust performance of CEP and HTV-SR compared to GFRP under identical conditions.

Although this study provides systematic understanding of corona aging mechanisms and comparative performance, several key challenges remain. Data-driven approaches that integrate PCA with machine learning or predictive modeling hold great potential for reliable lifetime assessment of polymeric insulators in high-voltage applications.

5 Conclusions

This study investigates the effects of AC corona discharge on a novel CEP developed for rigid insulator housings, in direct comparison with conventional composite insulator materials including HTV-SR and GFRP. The degradation behaviors of the materials were systematically analyzed in terms of surface morphology, molecular structure, elemental composition, and electrical properties under corona aging. PCA was subsequently applied to quantitatively evaluate the aging resistance of the materials. The main conclusions are as follows:

(1) Under corona aging, all three materials developed varying degrees of surface cracks and roughness. HTV-SR formed dense silica-like protective layers and exposed inorganic fillers that effectively suppressed further degradation. CEP exhibited carbonized resin and filler aggregation with relatively compact surface structures. GFRP underwent extensive matrix erosion and fiber exposure, with increased interfacial defects and void formation.

(2) FTIR and XPS analyses confirmed the occurrence of chain scission and oxidation in all materials. In HTV-SR, methyl side groups were oxidized to silanol, which further condensed into a crosslinked siloxane network. CEP exhibited epoxy ring-opening, accumulation of polar groups, and surface

carbonization. GFRP experienced more pronounced degradation of aromatic structures and polymer backbones. Corona aging resulted in marked reductions in DC flashover voltage, resistivity, and hydrophobicity across all materials, with GFRP showing the most severe deterioration, followed by CEP, while HTV-SR exhibited the highest stability.

(3) A PCA-based multi-parameter evaluation framework that links molecular-level chemical degradation pathways with macroscopic performance deterioration was established. The results show that both HTV-SR and CEP maintain relatively robust performance across multiple synergistic indicators, whereas GFRP suffers from pronounced interface degradation and matrix decomposition, leading to the weakest corona resistance. Overall, the cycloaliphatic epoxy resin exhibits superior aging resistance, structural stability, and electrical performance, positioning it as a promising alternative to traditional silicone rubber and epoxy composites for rigid insulator housings in high-voltage and harsh environmental applications.

Author contributions

Yuelin Liu: conceptualization, methodology, formal analysis and investigation, writing – original draft. Wendong Li: validation, resources, data curation. Shiyin Zeng: resources, data curation, conceptualization. Xinyi Yan: formal analysis and investigation. Haoyan Liu: visualization, methodology. Yuanyang Liu: resources, data curation. Guanjun Zhang: supervision, writing – review & editing, funding acquisition, project administration.

Conflicts of interest

There are no conflicts to declare.

Data availability

The data supporting this article have been included as part of the manuscript and it will be made available upon a reasonable request.

Acknowledgements

The authors kindly acknowledge the financial support of the Major Special Science and Technology Project of State Grid Henan Electric Power Company (Grant No. 521702240006) and Xiangyang Guowang Composite Insulators Co., Ltd., Hubei, China.

References

1 G. Wu, Y. Fan, Y. Guo, S. Xiao, Y. Liu, G. Gao and X. Zhang, Aging Mechanisms and Evaluation Methods of Silicone Rubber Insulator Sheds: A Review, *IEEE Trans. Dielectr. Electr. Insul.*, 2024, **31**, 965–979.

2 M. Akbar, R. Ullah and S. Alam, Aging of silicone rubber-based composite insulators under multi-stressed conditions: an overview, *Mater. Res. Express*, 2019, **6**, 102003.

3 G. Zhang, L. Zhao, R. Zhou, W. Shen and X. Liang, Review on Aging Characterization and Evaluation of Silicon Rubber Composite Insulator, *High Volt. Appar.*, 2016, **52**, 1–15.

4 M. Lu, C. Gao, Y. Yang, L. Li, C. Sheng and S. Zhang, Effect of bird pecking damage on operation performance of composite insulator, *Insul. Mater.*, 2024, **57**, 113–120.

5 X. Liang and Y. Gao, Study on Decay-Like Fracture of Composite Insulator: Part I- the Principal Character, Definition and Criterion of Decay-Like Fracture, *Proc. CSEE*, 2016, **36**, 4778–4786.

6 Y. Peng, W. Li, S. Zeng, Y. Zhang, Y. Deng, B. Peng, J. Liu, H. Yang and G. Zhang, Reproduction and Analysis of Decay-Like Aging Development Induced by Interfacial Discharge in Composite Insulators, *IEEE Trans. Dielectr. Electr. Insul.*, 2023, **30**, 1858–1867.

7 Y. Liu, Y. Lin, B. Cao, K. Wu and L. Wang, Enhancement of polysiloxane/epoxy resin compatibility through an electrostatic and van der Waals potential design strategy, *Polym. Test.*, 2023, **117**, 107820.

8 Y. Liu, Y. Lin, Y. Wang, K. Wu, B. Cao and L. Wang, Simultaneously improving toughness and hydrophobic properties of cycloaliphatic epoxy resin through silicone prepolymer, *J. Appl. Polym. Sci.*, 2022, **139**, e52478.

9 Y. Wang, Y. Liu, H. Mei, M. Xie and L. Wang, Research of cycloaliphatic epoxy resin and silicone rubber composite insulator interface based on four-electrode system and temperature rise model, *High Volt.*, 2023, **8**, 560–569.

10 L. Wang, Z. Nie, C. Zhao, J. Zhou and W. Geng, Water Permeation Characteristic in Cycloaliphatic Epoxy Resin Composite Insulator Sheath, *High Volt. Eng.*, 2019, **45**, 173–180.

11 X. Meng, R. Shang, H. Fan, Z. Wang, J. Cui, W. Diao, L. Wang and F. Yin, Aging Characteristics of Core Rod-sheath Interface of Alicyclic Epoxy Insulator and Silicone Rubber Composite Insulator Under Humid and Hot Environment, *Power Syst. Technol.*, 2023, **47**, 396–403.

12 X. Wang, H. Fan, W. Li, R. Shang, F. Yin and L. Wang, Effect of Ultraviolet—A Radiation on Alicyclic Epoxy Resin and Silicone Rubber Used for Insulators, *Polymers*, 2022, **14**, 4889.

13 L. Yin, C. Zhang, W. Yang, Y. Tian and B. Yan, Research on Impact-resistance Mechanical Characteristics of Shed Sheath Material of Composite Insulator, *High Volt. Appar.*, 2023, **59**, 44–53.

14 H. Xu, C. Xie, R. Wang, B. Gou, S. Luo and J. Zhou, Effects of electrical-hydrothermal aging degradation on dielectric and trap properties of high temperature vulcanized silicone rubber materials, *RSC Adv.*, 2020, **10**, 3805–3816.

15 Y. Deng, B. Peng, Z. Liu, Y. Du, S. Zhou, J. Liu, X. Yu and J. Zhou, Hygrothermal ageing performance of high temperature vulcanised silicone rubber and its degradation mechanism, *High Volt.*, 2023, **8**, 1196–1205.

16 M. Bi, R. Qiu, S. Duan, R. Deng, X. Chen and T. Jiang, Effects of Hygrothermal Conditions on Corona Aging of Silicone

Rubber, *IEEE Trans. Dielectr. Electr. Insul.*, 2025, **32**, 992–1000.

17 Y. Zhu, Influence of corona discharge on hydrophobicity of silicone rubber used for outdoor insulation, *Polym. Test.*, 2019, **74**, 14–20.

18 S. Zeng, W. Li, Y. Peng, Y. Zhang and G. Zhang, Mechanism of Accelerated Deterioration of High-Temperature Vulcanized Silicone Rubber under Multi-Factor Aging Tests Considering Temperature Cycling, *Polymers*, 2023, **15**, 3210.

19 Z. Zhang, T. Liang, Y. Xiang and X. Jiang, Effect of De-Powdering on the Performance of Silicone Rubber Composite Insulator, *Trans. China Electrotech. Soc.*, 2022, **37**, 2126–2135.

20 G. Pang, Z. Zhang, J. Li, S. Q. Li and S. M. Rowland, Effects of AC corona discharge on GFRP core rods used in composite insulators, *IEEE Trans. Dielectr. Electr. Insul.*, 2025, **32**, 2375–2384.

21 C. Zhang, J. Xiang, Z. Chen, Z. Wang, Y. Su, S. Wang, J. Li and S. Li, Surface degradation of epoxy resin exposed to corona discharge under bipolar square wave field: From phenomenon to the insights, *Polym. Degrad. Stab.*, 2024, **228**, 110922.

22 H. Fan, Y. Liu, L. Wang, F. Zhang, T. Wang and X. Zeng, Influence of Closing Joints of Epoxy Resin Insulator on Water Diffusion Test, *Power Syst. Technol.*, 2021, **45**, 2420–2426.

23 CIGRE WG D1.14, *Material Properties for Non-ceramic Outdoor Insulation: State of the Art, Technical Brochure No. 255*, 2004.

24 H. Hu, Z. Jia and X. Wang, Aging Mechanism of Silicone Rubber Under Thermal–Tensile Coupling Effect, *IEEE Trans. Dielectr. Electr. Insul.*, 2022, **29**, 185–192.

25 W. Bao, X. Liang, Y. Liu, Y. Gao and J. Wang, Effects of AC and DC corona on the surface properties of silicone rubber: characterization by contact angle measurements and XPS high resolution scan, *IEEE Trans. Dielectr. Electr. Insul.*, 2017, **24**, 2911–2919.

26 Y. Yang, Y. Wang, C. He, Z. Wang, X. Peng and P. Fang, Significantly Enhanced Corona Resistance of Epoxy Composite by Incorporation with Functionalized Graphene Oxide, *Materials*, 2024, **17**, 4864.

27 J. Yu, Y. Liu, B. Huang, L. Xia, F. Kong, C. Zhang and T. Shao, Rapid hydrophobicity recovery of contaminated silicone rubber using low-power microwave plasma in ambient air, *Chem. Eng. J.*, 2023, **465**, 142921.

28 J. Naveen, M. Sukesh Babu, R. Sarathi, R. Velmurugan, M. G. Danikas and A. Karlis, Investigation on Electrical and Thermal Performance of Glass Fiber Reinforced Epoxy–MgO Nanocomposites, *Energies*, 2021, **14**, 8005.

29 S. Zeng, W. Li, X. Zhao, Y. Peng, Y. Liu, X. Yan and G. Zhang, Degradation of HTV silicone rubber in composite insulators under UVB-corona coupling effect in simulated plateau environments, *Polym. Degrad. Stab.*, 2025, **238**, 111354.

30 H. Liu, G. Sun, Y. Liu, S. Zhang, C. Qi, S. Zhou, W. Li and G. Zhang, FlashSim: a novel particle-in-cell numerical model for vacuum surface flashover simulation based on finite element method, *Comput. Phys. Commun.*, 2025, **313**, 109625.

31 K. Shinozaki, M. Hikita, M. Kozako and M. Ueshima, in *2024 IEEE 5th International Conference on Dielectrics (ICD)*, 2024, pp. 1–4.

32 M. Bi, X. Rao, Y. Wen, H. Peng, T. Jiang and J. Tang, Study on Corona Aging Characteristics of Epoxy Resin Under Different Hygrothermal Environments, *IEEE Trans. Dielectr. Electr. Insul.*, 2023, **30**, 2249–2257.

33 X. Huang, W. Yang, Y. Tian and Z. Yuan, Effect of DC Corona Aging on Properties of HTV Silicone Rubber and Alicyclic Epoxy Resin, *Power Syst. Technol.*, 2020, **44**, 4454–4463.